

# Journal of Biomedical Optics

[SPIDigitalLibrary.org/jbo](http://SPIDigitalLibrary.org/jbo)

## **Near-ultraviolet removal rates for subgingival dental calculus at different irradiation angles**

Joshua E. Schoenly  
Wolf D. Seka  
Peter Rechmann

# Near-ultraviolet removal rates for subgingival dental calculus at different irradiation angles

Joshua E. Schoenly,<sup>a,b</sup> Wolf D. Seka,<sup>a,b</sup> and Peter Rechmann<sup>c</sup>

<sup>a</sup>University of Rochester, Laboratory for Laser Energetics, 250 East River Road, Rochester, New York 14623-1299

<sup>b</sup>University of Rochester, The Institute of Optics, Wilmot Building, 275 Hutchison Road, Rochester, New York 14627-0186

<sup>c</sup>University of California at San Francisco, School of Dentistry, Department of Preventive and Restorative Dental Sciences, 707 Parnassus Avenue, San Francisco, California 94143

**Abstract.** The laser ablation rate of subgingival dental calculus irradiated at a 400-nm-wavelength, 7.4-mJ pulse energy, and 85- and 20-deg irradiation angles is measured using laser triangulation. Three-dimensional images taken before and after irradiation create a removal map with 6- $\mu\text{m}$  axial resolution. Fifteen human teeth with subgingival calculus are irradiated *in vitro* under a cooling water spray with an  $\sim 300\text{-}\mu\text{m}$ -diam, tenth-order super-Gaussian beam. The average subgingival calculus removal rates for irradiation at 85 and 20 deg are  $11.1 \pm 3.6$  and  $11.5 \pm 5.9$   $\mu\text{m}/\text{pulse}$ , respectively, for depth removal and  $4.5 \pm 1.7 \times 10^5$  and  $4.8 \pm 2.3 \times 10^5$   $\mu\text{m}^3/\text{pulse}$ , respectively, for volume removal. The ablation rate is constant at each irradiation site but varies between sites because of the large differences in the physical and optical properties of calculus. Comparison of the average depth- and volume-removal rates does not reveal any dependence on the irradiation angle and is likely due to the surface topology of subgingival calculus samples that overshadows any expected angular dependence. © 2011 Society of Photo-Optical Instrumentation Engineers (SPIE). [DOI: 10.1117/1.3564907]

Keywords: selective ablation; subgingival; calculus; laser triangulation; frequency-doubled Ti:sapphire lasers; light microscopy; super-Gaussian.

Paper 10535SSP received Sep. 30, 2010; accepted for publication Dec. 3, 2010; published online Jul. 7, 2011.

## 1 Introduction

Dental calculus (tartar or mineralized dental plaque) is selectively ablated when irradiated with laser light at near-ultraviolet [(NUV), 300–400 nm] wavelengths with little to no removal of the surrounding healthy hard tissue (i.e., enamel, dentin, and cementum).<sup>1–3</sup> Scaling and root-planing tools in the dental clinic typically damage the underlying healthy hard tissue. This is problematic when removing subgingival calculus, where removal of healthy root cementum prohibits reattachment of fibroblasts for optimal healing. NUV lasers are a promising clinical tool that, unlike near-infrared lasers (e.g., Er:YAG and Er,Cr:YSGG), quickly remove calculus without removing any of the surrounding and underlying healthy hard tissue.

The NUV selective ablation mechanism of dental calculus is determined by its unique optical and physical properties compared to those of healthy hard tissue. Dental calculus is plaque that has been mineralized by deposited calcium and phosphate minerals originating from either the saliva or the gingival sulcus fluid.<sup>4</sup> The formation of its various mineral phases and bacterial composition depends on pH, the calcium-to-phosphate ratio, and location within the mouth.<sup>5</sup> Supragingival calculus occurs mainly near salivary gland openings into the mouth and is yellowish and softer, whereas subgingival calculus consists of hard dark crusts additionally influenced by exuded serum or blood components.<sup>6</sup> Although the absorption coefficient of dental calculus has not been measured at 400 nm, it is clear from the fluorescence excitation spectrum that calculus absorbs light at

this wavelength. The highest fluorescence emission for calculus occurs between 570 and 740 nm, with the highest excitation between 400 and 420 nm.<sup>7</sup> Some oral bacteria contain endogenous porphyrins absorbing near 400 nm and act as a photosensitizer, which if the wavelength of the incident light matches its peak absorption, it causes bacteria cell death through a photochemical mechanism.<sup>8,9</sup> The preferential absorption at 400 nm by porphyrins within some oral bacteria is one factor that may contribute to the selective ablation of calculus because healthy hard tissue will have only oral bacteria attached to the surface. It is easier to remove calculus because its Vickers hardness is an order of magnitude lower than that of enamel.<sup>10</sup>

Extensive *in vitro* research has been performed to remove carious tissue in the NUV using a frequency-doubled alexandrite laser ( $\lambda = 377$  nm).<sup>11,12</sup> Carious dentin is removed at 11.7  $\mu\text{m}/\text{pulse}$ , whereas healthy dentin is removed at 0.2  $\mu\text{m}/\text{pulse}$  at a fluence of 4 J/cm<sup>2</sup>.<sup>12</sup> (Fluence is also called energy-flux density and energy density with units of energy per unit area.) Calculus can be selectively removed using either a frequency-doubled alexandrite or a frequency doubled Ti:sapphire laser ( $\lambda = 400$  nm).<sup>1,13</sup> In the latter case, the removal rate for subgingival dental calculus at 5.7 J/cm<sup>2</sup> is found to primarily vary between 2 and 9  $\mu\text{m}/\text{pulse}$  at 45- and 90-deg irradiation angles relative to the tooth's surface.<sup>14</sup> Pristine cementum irradiated for 10 min under similar irradiation conditions shows only craters, 15–50  $\mu\text{m}$  deep, corresponding to an equivalent removal rate three orders of magnitude smaller than that obtained for calculus. Pristine enamel is not removed under the same irradiation conditions.

Address all correspondence to: J. E. Schoenly, Laboratory for Laser Energetics, University of Rochester, 250 East River Road, Rochester, New York 14623-1299. Tel: 585-275-5101; Fax: 585-275-5960; E-mail: jscho@lle.rochester.edu

Various optical methods, such as optical microscopy,<sup>15</sup> optical coherence tomography,<sup>16</sup> and laser triangulation,<sup>17</sup> have been used to determine ablation rates in dental hard tissue. The last method creates 3-D surface maps by projecting a laser line onto an optically rough surface and measuring the deviations on an inclined camera. Laser triangulation/profilometry has been used to measure crater depths in enamel from Er:YAG laser irradiation.<sup>17</sup> Removal maps are formed by subtracting the triangulation images measured before and after irradiation. The removal rate is obtained by controlling the number of incident pulses. This method calculates both depth and volumetric removal rates because triangulation measures a 3-D image of the tooth surface.

The location of subgingival calculus within a periodontal pocket requires that the irradiation angle of the surgical tool (i.e., an optical fiber, in this case) be oriented nearly parallel to the tooth's surface. Subgingival calculus is removed below the gum line, where the periodontal pocket has a clearance diameter of  $\leq 0.7$  mm; thus, the optical fiber must be oriented nearly parallel to the tooth's surface (e.g.,  $\leq 15$ – $20$  deg). The fluence, on a flat surface, decreases with irradiation angle  $\theta_{\text{irr}}$  as  $\cos[(\pi/2) - \theta_{\text{irr}}]$  because the laser beam is being stretched as a result of keystone distortion. Because the ablation rate depends on the incident fluence,<sup>18,19</sup> the removal rates for irradiation at  $20$  deg should be significantly lower than at  $85$  deg for the same pulse energy.

In this work, the ablation rates for subgingival calculus irradiated with a frequency-doubled Ti:sapphire laser (400-nm wavelength, 60-ns pulse duration, 10-Hz repetition rate) are measured using laser triangulation. Images of calculus removal during irradiation are documented using light microscopy to complement the 3-D triangulation images. The peak fluence incident on the tooth is analyzed by a method that takes into account the measured intensity distribution on the tooth's surface.

## 2 Materials and Methods

The frequency-doubled Ti:sapphire laser ( $\lambda = 400$  nm, 60-ns pulse duration, 10-Hz repetition rate) used in all calculus ablation experiments presented here has been described previously.<sup>2</sup> The experimental setup is shown in Fig. 1. The laser output was coupled into an optical fiber, with an input diameter tapered from 1800 to 600  $\mu\text{m}$ , using a  $\Delta\theta = 0.5^\circ$  engineered diffuser (RPC Photonics, Rochester, New York) and an  $F = 7.5$ -cm lens. A tapered input minimizes damage on the input surface by

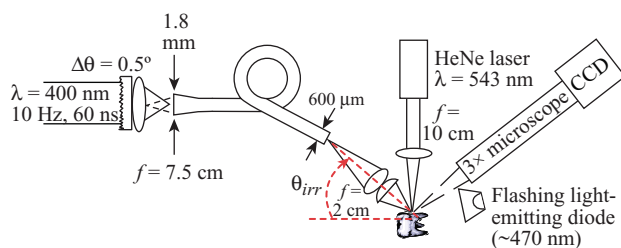


**Fig. 1** Optical setup used to irradiate teeth. The 400-nm laser is coupled into a tapered step-index fiber using an engineered diffuser and  $F = 7.5$ -cm lens. Laser triangulation is performed using a green HeNe laser line and a  $3\times$  microscope. Light microscope images use the profilometer camera with illumination from a flashing, blue-light-emitting diode.

allowing a larger intensity distribution with lower peak fluence on the input surface. The optical fiber was coiled around a 4-in.-diam drum to homogenize the intensity distribution at the output surface. The output from the fiber was imaged onto the tooth surface using an  $F = 2$ -cm objective to increase the peak fluence on the tooth surface without increasing the pulse energy. The intensity distribution at the image plane corresponded to a 300- $\mu\text{m}$ -diam, tenth-order super Gaussian. Variation of the intensity distribution and, consequently, the fluence, through focus was observed using a charge-coupled-device (CCD) camera (TM-1020A-15CL, JAI Inc., San Jose, California) and analyzed using MATLAB. The peak fluence at the image plane was  $6.1 \text{ J/cm}^2$  at normal incidence with a 7-mJ pulse energy. The irradiation laser was aligned before each experiment by observing an attenuated irradiation beam using the triangulation camera and a micrometer screw to set the best focus position. During the experiment, each tooth was irradiated at an angle  $\theta_{\text{irr}}$  either 85 or 20 deg relative to the tooth surface and cooled with a water spray ( $\sim 3$  ml/min).

The intensity distribution within 1 mm from the fiber output has been shown<sup>13</sup> to be an  $n$ 'th-order super-Gaussian of the form

$$I(r) = I(0) \exp(-r^n/w^n), \quad (1)$$

where  $I(r)$  is the intensity at radius  $r$ ,  $I(0)$  is the intensity at the center of the distribution,  $n$  is the order of super Gaussian, and  $w$  is the width of the distribution related to the full width at half maximum (FWHM) by  $\text{FWHM} = 2w(\sqrt[n]{\ln 2})$ . Because Eq. (1) is cylindrically symmetric,  $I(0)$  is the peak intensity (i.e., where the intensity is the highest). The fluence distribution  $F(r)$  can be substituted for  $I(r)$  in Eq. (1) because the intensity distribution varies little over time.

A total of 15 teeth with subgingival calculus were irradiated *in vitro*. The teeth were obtained from the Department of Preventive and Restorative Dental Sciences, School of Dentistry at the University of California, San Francisco. They were sterilized with gamma radiation and stored in a 0.1% thymol solution.

The number of laser pulses was regulated using a shutter control in the laser cavity. The shutter control (developed at the Laboratory for Laser Energetics) operated in five-pulse bursts. Between irradiation steps, images of the tooth were taken with side illumination from a flashing blue-light-emitting diode [(LED),  $\lambda \sim 450$ – $490$  nm] using the profilometer camera (see Fig. 1).

The depth of calculus removed by laser ablation was determined using a laser profilometer measuring a 3-D surface image of the tooth before and after irradiation. The two 3-D images were subtracted from each other, and a 3-D removal map was obtained. An  $800 \times 3054$ - $\mu\text{m}$  area of the tooth was typically scanned using a computer-controlled, motorized  $x$ - $y$ - $z$  stage (26449-05 stepper motors, Haydon Switch and Instrument, Waterbury, Connecticut). In laser profilometry, an axial variation from a reference  $Z$  to new depth  $Z'$  corresponds to a lateral deviation in the image plane of the CCD camera from  $X_I$  to  $X'_I$ . This axial variation, found from the geometry in Fig. 2(a), is given as

$$|Z - Z'| = \frac{|X_I - X'_I|}{m} \csc \theta, \quad (2)$$

where  $m$  is the magnification of the imaging lens and  $\theta$  is the angle between the incident laser and diffuse reflection at the refer-

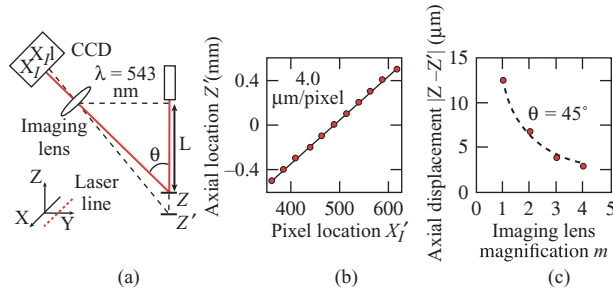


**Fig. 2** (a) Geometry of laser triangulation. An axial deviation in the object plane (from  $Z$  to  $Z'$ ) corresponds to a lateral deviation in the image plane (from  $X_i$  to  $X'_i$ ). The object coordinate system is shown to the lower left. (b) The axial displacement per pixel is determined by axially moving the object by several known displacements (filled circles). (c) The axial displacement per pixel of the laser profilometer as a function of imaging lens magnification. The data are best fit to a 45-degree triangulation angle.

ence position. A  $0.75\times$  to  $4\times$  zoom microscope lens (VZM450i, Edmund Industrial Optics, Barrington, New Jersey) was used as the imaging lens, along with a CCD camera (TM-1020A-15CL, JAI, San Jose, California). A HeNe laser ( $\lambda = 543$ -nm, model LHGR-0050, PMS Electro-Optics, Boulder, Colorado) was used as the primary laser for the profilometer and was focused to a line onto the tooth surface using an  $F = 10$ -cm cylindrical lens. The axial displacement per pixel is determined by moving the sample by a known displacement as shown in Fig. 2(b). At the  $3\times$  magnification used in this experiment, the axial displacement per pixel was  $\sim 4$   $\mu\text{m}/\text{pixel}$ . The axial displacement per pixel was determined at different magnifications to verify Eq. (2), as shown in Fig. 2(c). Fitting the data from Fig. 2(c) to Eq. (2), the camera inclination angle,  $\theta$ , was verified to be 45 deg. The FWHM of the laser line was  $\sim 20$   $\mu\text{m}$ . The  $X$ - $Y$ - $Z$  resolution in tooth coordinates for a lineout of the single pixel width was  $60\times 40\times 6$   $\mu\text{m}$ .

The removal images were improved by performing speckle reduction during image acquisition and spatial filtering in post-image processing. The triangulation laser was passed through a  $\Delta\theta = 0.5$  deg, 50-rpm rotating holographic diffuser (NT47-989, Edmund Industrial Optics, Barrington, New Jersey) to reduce the speckle in the laser line. Speckle noise was further reduced using digital filtering.

### 3 Results

#### 3.1 Determination of Fluence

The fluence distribution is found by measuring the intensity distribution at the tooth surface with a CCD camera. Because the intensity distribution varies little between laser shots, fluence is assigned to each pixel upon measurement of the pulse energy. For a smooth, super-Gaussian intensity distribution from Eq. (1), the peak fluence  $F_P$  is located at the center of the distribution. Adding Gaussian noise to a computer-generated image [Fig. 3(a)] better represents what was experimentally measured at normal incidence when directing an attenuated laser beam into a CCD camera [Fig. 3(b)]. A 7-mJ pulse energy is assumed in each image. In either case, assigning  $F_P$  with the largest fluence in the image was not realistic because the measurement includes

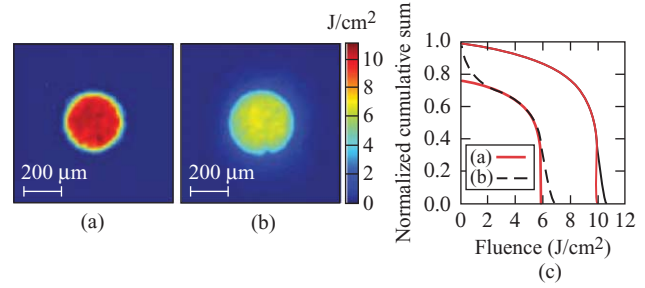


**Fig. 3** (a) A computer-generated image of a 300- $\mu\text{m}$ -diam (FWHM), tenth-order super Gaussian. Gaussian noise is added in (a) to best reflect what is experimentally measured in (b). (c) The NCS of the fluence distribution in images (a) and (b) [solid and dotted black lines, respectively]. The solid normalized line is  $\eta_{CS}$  for a tenth-order super Gaussian. A pulse energy of 7 mJ is assumed in each image. The difference between (a) and (b) is that in (b) experimental optical aberrations are included.

noise. Examining the normalized cumulative sum (NCS) of the fluence distributions in Figs. 3(a) and 3(b) [see Fig. 3(c)], a common structure is observed in each curve. This common underlying curve is fit to

$$\eta_{CS}(r_F) = 1 - \frac{\Gamma[(2/n), -\ln r_F]}{\Gamma[(2/n), 0]}, \quad (3)$$

where  $\eta_{CS}(r_F)$  is the NCS for a smooth,  $n$ 'th-order super-Gaussian fluence distribution,  $r_F$  is a fluence ratio normalized to the peak fluence ranging from 0 to 1 and  $\Gamma(a, x)$  is the upper incomplete gamma function. [The upper incomplete Gamma function  $\Gamma(a, x)$  is defined here as  $\Gamma(a, x) = \int_x^\infty e^{-t} t^{a-1} dt$ . The complete gamma function  $\Gamma(a)$  is by definition  $\Gamma(a) = \Gamma(a, 0)$ . The fraction on the right-hand side of Eq. (3) is also known as the regularized upper incomplete gamma function.] Equation (3) is derived from a 2-D cumulative sum of radii (which correspond to fluences because the equation is cylindrically symmetric) in Eq. (1) normalized to a 2-D integral of Eq. (1) over all space. Equation (1) is more compact than what has been derived previously allowing for a 1000 $\times$  faster computation time.<sup>14</sup> The common underlying curve for the NCS of the images in Figs. 3(a) and 3(b) is fit to  $\eta_{CS}$  in Eq. (3) for a tenth-order super Gaussian [red lines in Fig. 3(c)]. The red lines overlap the common underlying curve of the NCS generated from the computer-generated image [Fig. 3(a)] and the experimental image [Fig. 3(b)]. The highest and lowest fluences, where  $\eta_{CS}$  and the NCS do not overlap, correspond to noise or aberrations within the beam and background, respectively. The intersection of  $\eta_{CS}$  with the  $x$ -axis of the NCS from Figs. 3(a) and 3(b) corresponds to  $F_P$  for a smooth distribution. The fluence at the inflection point (toward the highest fluences) of the NCS for Figs. 3(a) and 3(b) is approximately  $F_P$  and is found by taking the derivative of the NCS. The fluences reported in this paper correspond to this fluence value.

#### 3.2 Measurement of Removal Rates

Subgingival calculus is removed when it is irradiated at 6.3  $\text{J}/\text{cm}^2$  and 85 deg (shown in Fig. 4). Sequential light microscope images in five-pulse increments from 0 to 25 pulses are shown in Figs. 4(a)–4(f). Differential removal maps (i.e., incremental changes in calculus removed instead of total calcu-

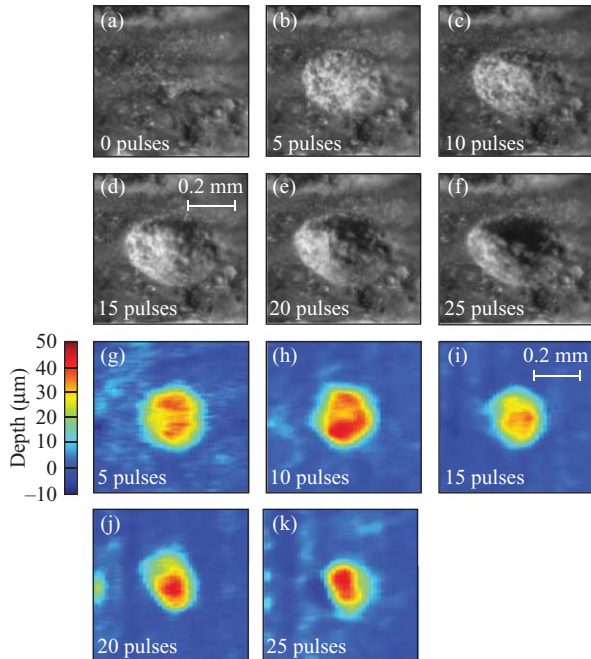


**Fig. 4** Light microscope images of total calculus removal (a) before and after (b) 5, (c) 10, (d) 15, (e) 20, and (f) 25 irradiation pulses at 6.3 J/cm<sup>2</sup> and 85 deg. Differential removal maps of incremental calculus removal at five-pulse increments after (g) 5, (h) 10, (i) 15, (j) 20, and (k) 25 irradiation pulses corresponding to the above light microscope images. The scales in (d) and (i) are the same for all images.

lus removed) are shown below their respective light microscope images in Figs. 4(g)–4(k) in five-pulse increments. Depth- and volume-removal rates for the images in Fig. 4 are shown in Fig. 5. Depth and volume removed in each graph in Fig. 5 are determined as cumulative removal from the differential removal maps in Figs. 4(g)–4(k). The depth removed is the peak depth in each differential removal map. Volume removed is defined within the area where depths removed are  $\geq 3 \times$  the standard deviation of the background noise. Although the removal areas in Figs. 4(g)–4(k) look to be decreasing as removal progresses, the decrease is minimal as a linear trend is observed in both plots in Fig. 5, resulting in a depth- and volume-removal rate of 8.0  $\mu\text{m}/\text{pulse}$  and  $4.2 \times 10^5 \mu\text{m}^3/\text{pulse}$ , respectively.

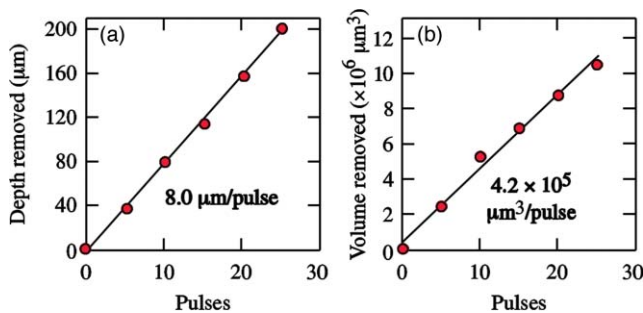


**Fig. 5** Plotting (a) depth and (b) volume of calculus removed as a function of the number of irradiation pulses at 6.3 J/cm<sup>2</sup> and 85 deg. The trend line in each image is a linear least-squares fit to the data points including the origin. Removal rates are 8.0  $\mu\text{m}/\text{pulse}$  and  $4.2 \times 10^5 \mu\text{m}^3/\text{pulse}$  for depth and volume removed, respectively.

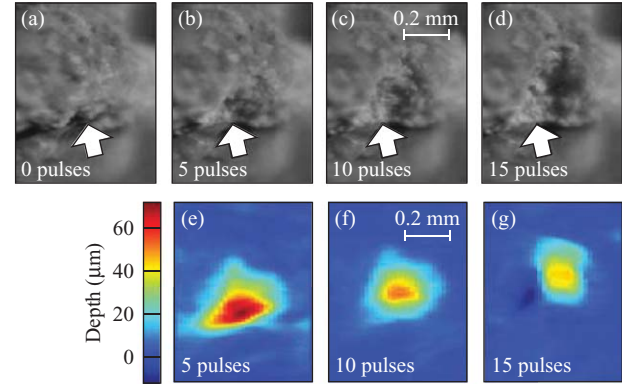


**Fig. 6** Light microscope images of total calculus removal (a) before and after (b) 5, (c) 10, and (d) 15 irradiation pulses at 7.3 mJ and 20 deg. The white arrows show the direction and angle of the irradiation laser. Differential removal maps of incremental calculus removal at five-pulse increments after (e) 5, (f) 10, and (g) 15 irradiation pulses corresponding to the above light microscope images. The scales in (c) and (f) are the same for all images. Negative removal to the left of the main spot in (g) is due to a minor obstruction.

Light microscope images in Figs. 6(a)–6(d) illustrate removal of subgingival calculus at a 7.3-mJ pulse energy and 20-deg irradiation angle. Correcting for the irradiation angle, the peak fluence is determined to be 2.2 J/cm<sup>2</sup> (at normal incidence, the peak fluence is 6.4 J/cm<sup>2</sup>). Differential removal maps are shown in Figs. 6(e)–6(g) in five-pulse increments below the corresponding light microscope images. Negative removal to the left of the main spot in Fig. 6(g) is indicative of obstructions inherent of a laser triangulation measurement. These obstructions result from a deep crater where the laser line is no longer seen by the camera, leaving gaps in the line where these obstructions occur. Depth- and volume-removal plots for Fig. 6 are shown in Fig. 7. Data points for either depth or volume removed indicate a linear trend of 10.8  $\mu\text{m}/\text{pulse}$  and  $5.3 \times 10^5 \mu\text{m}^3/\text{pulse}$ , respectively. In this case, removal maps after 15 pulses were inaccurate because obstruction becomes more of a problem as the crater deepened.

Depth- and volume-removal rates obtained from the 15 teeth with subgingival calculus are summarized in the box-and-whisker plots in Fig. 8, which compared irradiation angles of 85 and 20 deg. There were 23 and 17 measurements taken at 85 and 20 deg, respectively. The whisker length was 1.5 $\times$  the

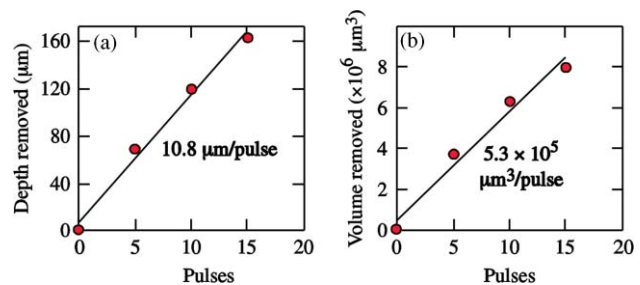


**Fig. 7** Plotting (a) depth and (b) volume of calculus removed as a function of the number of irradiation pulses at 7.3 mJ and 20 deg. The trend line in each image is a linear least-squares fit to the data points including the origin. Removal rates are 10.8  $\mu\text{m}/\text{pulse}$  and  $5.3 \times 10^5 \mu\text{m}^3/\text{pulse}$  for depth and volume removed, respectively.

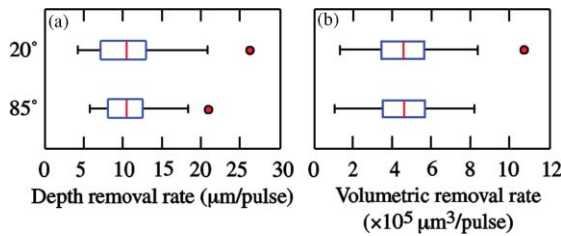


**Fig. 8** Box-and-whisker plots for (a) depth- and (b) volume-removal rates at 20- and 85-deg irradiation angles and 7.3- and 7.5-mJ average pulse energies, respectively. Data points contained in the blue boxes are within the 25th to 75th percentile of the data set. The whiskers are defined as  $1.5 \times$  the interquartile range and the red dots are outliers. The vertical line within each box is the median.

interquartile range. The red lines within the boxes are the median of the distribution, and the red dots are outliers. Statistical results for these distributions are shown in Table 1. The median removal rate is also reported because it is less sensitive to a skewed distribution compared to an average/mean removal rate. There is no apparent dependence on the irradiation angle when comparing both depth- and volume-removal rates at 85 and 20 deg, where the mean and median removal rates are nearly identical (see Table 1).

#### 4 Discussion

Evaluating the NCS over a fluence distribution is a novel metric to determine the peak fluence and underlying shape of the distribution (i.e., order of super Gaussian). A common method used to determine  $F_P$  is to fit a slice through the center of the beam to a Gaussian or super-Gaussian function [see Eq. (1)]. On measurement of the width  $w$  of the slice [as defined in Eq. (1)], the peak fluence  $F_P$  can be determined using

$$F_P = \frac{E_{\text{laser}}}{\left(\frac{2}{n}\right) \pi w^2 \Gamma\left(\frac{2}{n}\right)}, \quad (4)$$

where  $E_{\text{laser}}$  is the laser pulse energy,  $n$  is the order of super Gaussian, and  $\Gamma(a)$  is the complete gamma function. This method assumes the fluence distribution is rotationally symmetric and contains no aberrations. The NCS method uses the entire fluence distribution instead of just a slice through the center of the beam. Comparing the computer-generated curve in Fig. 3(a) to the measured image in Fig. 3(b), the peak fluence is significantly

higher for the former. This is mainly due to optical aberrations from the irradiation lens, which create a distribution of lower fluences surrounding the main beam and reduce the peak fluence. Using the NCS method to determine the shape and peak fluence of the distribution requires accurate measurement of the intensity distribution and appropriate background subtraction. It was found in image processing that low-pass filtering the image and using a binary mask to remove the background noise provided the most repeatable results for the peak fluence. A slightly lopsided, zero-average, Gaussian noise distribution necessitated the use of a binary mask because the NCS was highly dependent on the crop size of the image because the background noise did not cancel after summation. Applying an appropriate low-pass filter before applying the mask ensured that low signal data were not removed along with the background noise.

The NCS for an  $n$ 'th-order super-Gaussian distribution  $\eta_{\text{CS}}$  in Eq. (3) is related mathematically to the energy efficiency for selective ablation  $\eta_E$ , introduced in previous papers,<sup>2,13</sup> but not conceptually related. The energy efficiency for selective ablation is defined as

$$\eta_E = \frac{E_{\text{abl}}}{E_{\text{laser}}} = \eta_{\text{CS}} \left( \frac{F_{\text{ca}}}{F_P} \right), \quad (5)$$

where  $E_{\text{abl}}$  is the energy used for selective ablation and  $F_{\text{ca}}$  is the fluence ablation threshold for calculus/caries. While  $\eta_{\text{CS}}$  is a general function of fluence ratios  $r_F$  from 0 to 1,  $\eta_E$  is  $\eta_{\text{CS}}$  evaluated at only one fluence ratio  $r_F = F_{\text{ca}}/F_P$ .

Blue-light microscopy is a qualitative diagnostic that complements the quantitative measurements from laser profilometry in evaluating the removal rate (see Figs. 4 and 6). Profilometer images do not discriminate healthy hard tissue and photobleached calculus from dental calculus, whereas the light microscope images provide this information. Photobleaching information can be obtained because the NUV chromophores in the calculus are absorbed by blue LED ( $\lambda \sim 450\text{--}490$  nm) illumination. Differentiating between the scenarios where either the underlying hard tissue had been reached or the calculus had been photobleached solely from the profilometer traces would not be possible because both cases result in zero calculus removal.

Laser ablation of subgingival calculus at 400 nm and  $6.4 \text{ J/cm}^2$  exhibits a linear rate of depth and volume removed, even though this linear removal rate varies between irradiation sites (e.g., see Figs. 5 and 7). The maximum depths removed were of the order of  $\approx 200 \mu\text{m}$  in 20–30 pulses. Most irradiation sites at either irradiation angle exhibited a linear trend of calculus removal. Investigation of this linear trend at deeper

**Table 1** Statistical data for the removal rates measured in the experiment. There is little difference between average and median removal at 20 and 85 deg. Irradiation at 20 deg has a larger standard deviation of depth- and volume-removal rates compared to 85 deg. Assuming normal incidence, the associated fluence for 20 and 85 deg are  $6.4 \pm 0.1$  and  $6.5 \pm 0.1 \text{ J/cm}^2$ .

Irradiation angle	Pulse energy (mJ)	Depth-removal rates ( $\mu\text{m}/\text{pulse}$ )			Volume-removal rates ( $\times 10^5 \mu\text{m}^3/\text{pulse}$ )		
		Mean	Median	Standard deviation	Mean	Median	Standard deviation
20 deg	$7.3 \pm 0.1$	11.5	10.5	5.9	4.8	4.6	2.3
85 deg	$7.5 \pm 0.1$	11.1	10.4	3.6	4.5	4.6	1.7

removal depths was difficult because the effect from triangulation obstructions became more pronounced and could not be corrected in postimage processing. Unless photobleaching occurs or the laser encounters a layer of calculus deficient in bacterial chromophores, calculus removal should still exhibit a linear trend at deeper removal depths.

The box-and-whisker plot (Fig. 8) of subgingival calculus-removal rates demonstrates the variability of calculus ablation among different teeth. The removal rate is typically a function of the incident fluence, the optical properties (e.g., the absorption coefficient), and the mechanical/physical properties (e.g., the density of the calculus and how strongly the calculus is attached to the tooth) of the target tissue. Even though the removal rate is constant over time, subgingival calculus compositionally varies among patients and locations within the oral cavity. Consequently, the number density of NUV optical absorbers within calculus (i.e., bacterial components forming plaque and calculus) varies, leading to a variation in the absorption coefficient and, subsequently, the removal rate. The absorption coefficient of dental calculus at 400 nm and its variation between different oral environments remains to be measured. It is apparent under blue-light illumination microscopy; however, that calculus has variable absorption based on varying contrast in these images. The density of dry dental calculus has been shown to vary between 1.3 and 1.9 mg/mm<sup>2</sup>.<sup>20</sup> The applied forces needed to remove subgingival dental calculus in scaling also vary as  $5.7 \pm 3.3$  N.<sup>21</sup> Similarly, outliers in the box-and-whisker plots in Fig. 8 may be due to weak mechanical forces attaching the calculus to the tooth (i.e., some calculus readily comes off in clumps rather than at a linear removal rate). These properties (i.e., absorption coefficient, density, and mechanical integrity) affect the ablation rate of subgingival calculus so that variations in these properties would account for the variation observed in Fig. 8.

Depth- and volume-removal rates for subgingival calculus removal at 20 and 85 deg do not suggest a dependence on the irradiation angle. Comparison of both average or median depth and volume rates in Table 1 indicates similar values for each angle. The fluence distribution incident on a surface is a function of the irradiation angle  $\theta_{\text{irr}}$  because the incident laser beam would be stretched as in Fig. 9(a). For a collimated beam, the peak fluence is reduced by a factor  $\cos[(\pi/2) - \theta_{\text{irr}}]$ . For  $\theta_{\text{irr}} = 20$  deg in Fig. 9(a), the fluence is reduced by a factor of 0.34 compared to  $\theta_{\text{irr}} = 90$  deg in Fig. 9(b). Although removal rate is a function of the fluence<sup>19</sup> and, therefore, of the irradiation angle, the surface topology of the calculus must be taken into account. The results in Table 1 are likely a result of irradiating the side of a calculus mound [Fig. 9(c)] as opposed to a sheet of calculus [Fig. 9(a)]. The former scenario occurred more often in this experiment; thus, it is not unusual that the removal rates in Table 1 are nearly identical between irradiation angles. Irradiating a thin sheet of calculus comparable to the scenario in Fig. 9(a) would be more difficult to remove owing to a reduction in the fluence. This difficulty was observed in this experiment, where the removal rate decreased when the irradiation scenario was similar to Fig. 9(a). Thick layers of calculus approximate more the scenario shown in Fig. 9(c).

Clear evidence of stalling from photobleaching was not observed in this experiment at 6.4 J/cm<sup>2</sup> and 85 deg. Observed in previous cases at lower fluences ( $\leq 2$  J/cm<sup>2</sup>) at 400 nm, stalling

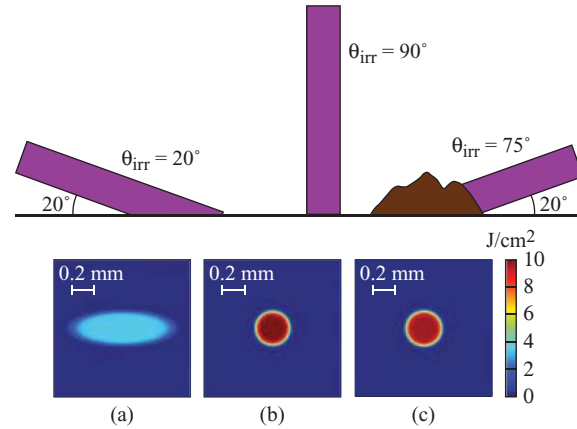


**Fig. 9** Schematic of different irradiation conditions pertinent to calculus ablation. (a) Standard irradiation at (a)  $\theta_{\text{irr}} = 20$  deg and (b)  $\theta_{\text{irr}} = 90$  deg. (c) Likely scenario for irradiating complex calculus topology at 20 deg. Below each scenario are the relevant, computer-generated intensity distributions for a 300- $\mu\text{m}$ -diam, 10th-order super Gaussian.

of selective ablation is caused by decreasing the number density of NUV absorbers within the calculus, making the calculus appear white under blue-light illumination.<sup>13</sup> Stalling is not a new phenomenon and has been observed when removing dental hard tissue using an Er:YAG laser at too low of a fluence.<sup>15,22</sup> Although stalling from photobleaching was not observed at 6.4 J/cm<sup>2</sup> in this experiment, it also has not been reported when using a 377-nm laser to remove dental calculus at a lower fluence of 1 J/cm<sup>2</sup>.<sup>1</sup> This may be due to experimental conditions where the teeth were not treated with gamma radiation; gamma radiation treatment may reduce the number density of NUV optical absorbers within the calculus and increase the likelihood of photobleaching. Future experiments are needed to compare the removal rates of teeth treated and not treated with gamma radiation.

## 5 Conclusion

The 400-nm irradiated depth- and volume-removal rates for subgingival dental calculus were measured and shown to be a function of irradiation angle when calculus topology was taken into account. These removal rates were measured using laser triangulation/profilometry. The teeth were irradiated at 85 and 20 deg to the tooth surface with a 7.4-mJ pulse energy (a 6.4-J/cm<sup>2</sup> fluence at 90 deg). The average removal rate for irradiation at 85 and 20 deg is  $11.1 \pm 3.6$  and  $11.5 \pm 5.9$   $\mu\text{m}/\text{pulse}$ , respectively, for depth removal and  $4.5 \pm 1.7 \times 10^5$  and  $4.8 \pm 2.3 \times 10^5$   $\mu\text{m}^3/\text{pulse}$ , respectively, for volume removal. The large uncertainty in the removal rate reflects the biological variability in the formation of subgingival calculus resulting in a variation of its optical and mechanical properties. These results indicate that it is not always necessary to increase the pulse energy when the irradiation fiber is oriented nearly parallel to the tooth surface because the fluence will also depend on calculus topology.

## Acknowledgments

This work was supported by the U.S. Department of Energy Office of Inertial Confinement Fusion under Cooperative Agreement No. DE-FC52-08NA28302, the University of Rochester,

and the New York State Energy Research and Development Authority. The support of DOE does not constitute an endorsement by DOE of the views expressed in this article.

## References

1. P. Rechmann and T. Hennig, "Selective ablation of sub- and supragingival calculus with a frequency-doubled alexandrite laser," *Proc. SPIE* **2394**, 203–210, (1995).
2. J. E. Schoenly, W. Seka, and P. Rechmann, "Laser ablation of dental calculus at 400 nm using a Ti:sapphire laser," *Proc. SPIE* **7162**, 71620E (2009).
3. P. Rechmann, "Selective ablation of dental calculus with frequency-doubled alexandrite laser," *Proc. SPIE* **2623**, 180–188 (1996).
4. J. Hayashizaki, S. Ban, H. Nakagaki, A. Okumura, S. Yoshii, and C. Robinson, "Site specific mineral composition and microstructure of human supra-gingival dental calculus," *Arch. Oral. Biol.* **53**, 168–174 (2008).
5. P. Marsh and M. Martin, *Oral Microbiology*, 4th ed., p. 193, Oxford, Boston (1999).
6. E. A. Roberts-Harry and V. Clerehugh, "Subgingival calculus: where are we now? A comparative review," *J. Dent.* **28**, 93–102 (2000).
7. W. Buchalla, A. M. Lennon, and T. Attin, "Fluorescence spectroscopy of dental calculus," *J. Periodontol. Res.* **39**(5), 327–332 (2004).
8. O. Feuerstein, N. Persman, and E. I. Weiss, "Phototoxic effect of visible light on *porphyromonas gingivalis* and *fusobacterium nucleatum*: an *in vitro* study," *Photochem. Photobio.* **80**, 412–415 (2004).
9. T. Hennig, P. Rechmann, T. Pecnik, H.-P. Heinz, and U. Hadding, "Influence of second harmonic alexandrite-laser radiation on bacterial growth," *Proc. SPIE* **2672**, 40–50 (1996).
10. D. J. White, "Processes contributing to the formation of dental calculus," *Biofouling* **4**(1–3), 209–218 (1991).
11. T. Hennig, P. Rechmann, C. G. Pilgrim, H.-J. Schwarzmaier, and R. Kaufmann, "Caries selective ablation by pulsed lasers," *Proc. SPIE* **1424**, 99–105 (1991).
12. T. Hennig, P. Rechmann, P. Jeitner, and R. Kaufmann, "Caries-selective ablation: the second threshold," *Proc. SPIE* **1880**, 117–124 (1993).
13. J. E. Schoenly, W. Seka, and P. Rechmann, "Investigation into the optimum beam shape and fluence for selective ablation of dental calculus at  $\lambda = 400$  nm," *Lasers Surg. Med.* **42**, 51–61 (2010).
14. J. E. Schoenly, W. Seka, and P. Rechmann, "Selective near-UV ablation of subgingival dental calculus: Measurement of removal rates," *Proc. SPIE* **7549**, 754906 (2010).
15. D. Fried, J. Ragadio, M. Akrivou, J. D. B. Featherstone, M. W. Murray, and K. M. Dickenson, "Dental hard tissue modification and removal using sealed transverse excited atmospheric-pressure lasers operating at  $\lambda = 9.6$  and  $10.6 \mu\text{m}$ ," *J. Biomed. Opt.* **6**(2), 231–238 (2001).
16. M. Ohnishi, D. Takada, M. Ohmi, and M. Haruna, "Dynamic analysis of laser ablation of biological tissue using a real-time OCT," *Proc. SPIE* **7175**, 717513 (2009).
17. T. Perhavec, A. Gorkic, D. Bracun, and J. Diaci, "A method for rapid measurement of laser ablation rate of hard dental tissue," *Opt. Laser Technol.* **41**, 397–402 (2009).
18. A. Vogel and V. Venugopalan, "Mechanisms of pulsed laser ablation of biological tissues," *Chem. Rev.* **103**, 577–644 (2003).
19. R. Srinivasan, "Ablation of polymers and biological tissue by ultraviolet lasers," *Science* **234**, 559–565 (1986).
20. M. F. Little, C. A. Casciani, and J. Rowley, "Dental calculus composition. 1. Supragingival calculus: Ash, calcium, phosphorus, sodium, and density," *J. Dent. Res.* **42**, 78–86 (1963).
21. U. Zappa, J. Cadosch, C. Simona, H. Graf, and D. Case, "In vivo scaling and root planing forces," *J. Periodontol.* **62**(5), 335–340 (1991).
22. K. K. Sheth, M. Staninec, A. V. Sarma, and D. Fried, "Selective targeting of protein, water, and mineral in dentin using UV and IR pulse lasers: the effect on the bond strength to composite restorative materials," *Lasers Surg. Med.* **35**, 245–253 (2004).